

# High-resolution imaging of ultracold fermions in microscopically tailored optical potentials

B Zimmermann<sup>1,\*</sup>, T Müller<sup>1,\*</sup>, J Meineke<sup>1</sup>, T Esslinger<sup>1,†</sup> and H Moritz<sup>1,2</sup>

<sup>1</sup>Institute for Quantum Electronics, ETH Zürich, Hönggerberg, CH-8093 Zürich, Switzerland

<sup>2</sup>Institut für Laser-Physik, Universität Hamburg, Luruper Chaussee 149, D-22761 Hamburg, Germany

E-mail: [esslinger@phys.ethz.ch](mailto:esslinger@phys.ethz.ch)

**Abstract.** We report on the local probing and preparation of an ultracold Fermi gas on the length scale of one micrometer, i.e. of the order of the Fermi wavelength. The essential tool of our experimental setup is a pair of identical, high-resolution microscope objectives. One of the microscope objectives allows local imaging of the trapped Fermi gas of <sup>6</sup>Li atoms with a maximum resolution of 660 nm, while the other enables the generation of arbitrary optical dipole potentials on the same length scale. Employing a 2D acousto-optical deflector, we demonstrate the formation of several trapping geometries including a tightly focussed single optical dipole trap, a 4x4-site two-dimensional optical lattice and a 8-site ring lattice configuration. Furthermore, we show the ability to load and detect a small number of atoms in these trapping potentials. A site separation of down to one micrometer in combination with the low mass of <sup>6</sup>Li results in tunneling rates which are sufficiently large for the implementation of Hubbard-models with the designed geometries.

\* These authors contributed equally to the presented work.

† Author to whom any correspondence should be addressed.

## Contents

<b>1</b>	<b>Introduction</b>	<b>2</b>
<b>2</b>	<b>Preparation of a degenerate Fermi gas with high optical access</b>	<b>3</b>
<b>3</b>	<b>Optical system</b>	<b>5</b>
3.1	High-resolution microscope objectives . . . . .	5
3.2	Imaging setup . . . . .	7
3.3	Generation of optical micro-potentials . . . . .	7
<b>4</b>	<b>Optical micro-potentials</b>	<b>8</b>
4.1	Single spot micro-trap . . . . .	8
4.2	Multiple spot micro-traps . . . . .	9
<b>5</b>	<b>Atoms in micro-potentials</b>	<b>11</b>
<b>6</b>	<b>Conclusion and outlook</b>	<b>13</b>
	<b>Acknowledgments</b>	<b>14</b>
	<b>References</b>	<b>14</b>

## 1. Introduction

Ultracold atomic Fermi gases provide a unique opportunity to create strongly correlated many-body systems and to study intriguing phenomena, such as the crossover between Bose-Einstein condensation and Bardeen-Cooper-Schrieffer superfluidity [1]. Experimental access to this physics at a microscopic scale is now within reach as tools are being developed to manipulate and observe quantum gases with high spatial resolution [2, 3, 4]. For a fermionic system, a fundamental length scale is set by the Fermi wavelength  $\lambda_F$ , which for instance determines the interparticle distance and the scaling of density-density correlations. Typically,  $\lambda_F$  is of the order of one micrometer, a length scale which is accessible by optical means.

Indeed, local optical probing has recently already allowed the in-situ observation of suppressed density fluctuations in a degenerate Fermi gas [5]. Extending this technique to local measurements of density or spin fluctuations on the microscopic length scale of the interatomic distance should give direct access to magnetic properties [6, 7] and second-order, long-range correlations [8], such as the pair correlations characterizing a superfluid Fermi gas. Thus, the ability to probe ultracold Fermi gases on their natural length scale, the Fermi wavelength, will permit to gain deeper insight into the mechanisms governing strongly correlated systems.

The manipulation of cold atoms on microscopic scales can be accomplished with optical lattices [9, 10]. Ultracold fermions in optical lattices constitute an almost ideal

experimental realization of the Hubbard model with highly tunable parameters [11], and very recently even single site resolution imaging has been achieved for bosonic systems [12, 13, 14]. Yet, the concept of optical lattices is by design restricted to the investigation of periodic systems with a high degree of symmetry. Various approaches towards more arbitrary, locally controllable geometries for optical potentials have been successfully reported, for example double wells [15, 16], ring traps [17, 18], ring lattices [18, 19], box potentials [20] and finite lattice patterns [18, 19, 21]. However, most realizations so far still lack the ability to shape optical potentials on length scales comparable to the interatomic distance. Hence, tunneling processes and dynamics are correspondingly very slow. To our knowledge, experiments with fermions in microscopically tailored optical potentials have not been reported yet.

In this work, we present the combination of both, the detection as well as the preparation of ultracold fermionic samples on the microscopic length scale of the Fermi wavelength. The main feature of our new experimental apparatus is a pair of identical microscope objectives, each with an optical resolution of 660 nm at a wavelength of 671 nm. One microscope objective is part of a high-resolution imaging setup, while the other is used for shaping versatile optical dipole potentials, which can be tailored down to length scales below one micrometer. Using a two-axis acousto-optical deflector, we demonstrate the site-by-site creation and characterization of a tightly focussed single optical dipole trap, a 4x4-site two-dimensional square lattice and a 8-site ring lattice structure. Moreover, we show the spatially resolved imaging of cold atoms residing in the optically projected potential patterns.

## 2. Preparation of a degenerate Fermi gas with high optical access

We first outline the experimental concept of generating a quantum degenerate Fermi gas of  ${}^6\text{Li}$  atoms, which is used as a reservoir for loading atoms into the optical micro-potentials (see sections 4 and 5). Details on the experimental setup are given in [22].

Our experimental apparatus consists of four sections which are schematically depicted in figure 1: The oven chamber, the Zeeman slower, the main ultra-high vacuum (UHV) chamber containing a high finesse optical resonator, and the octagonal UHV glass cell attached to the main vacuum chamber. The glass cell constitutes the final science chamber offering high optical access for the microscopic detection and manipulation of ultracold fermions. The preparation procedure of the degenerate quantum gas - as illustrated in figure 1(a)-(d) - has a duty cycle of approximately 12s and follows an all-optical approach, similar to the methods applied in [23]:  ${}^6\text{Li}$  atoms emanating from the oven are decelerated by a Zeeman slower and subsequently captured in a magneto-optical trap (MOT) at the center of the main UHV chamber (see figure 1(a)). After 4s of loading, the MOT typically contains  $10^9$  atoms at a temperature of about  $200 \mu\text{K}$ . In a second step, up to  $9 \cdot 10^7$  atoms are transferred into a large-volume standing-wave optical dipole trap realized by the high-finesse optical resonator inside the main vacuum chamber (see figure 1(b)). It consists of one flat and one curved mirror (radius of

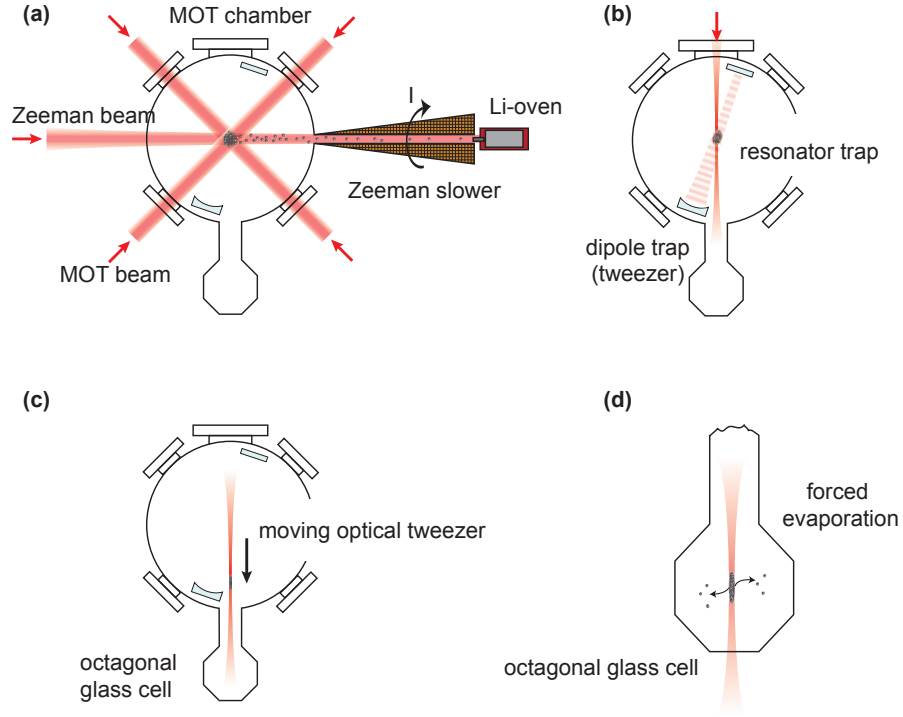


**Figure 1.** Experimental cycle: (a)  ${}^6\text{Li}$  atoms, emerging from the oven, are decelerated by a Zeeman slower and captured in a magneto-optical trap. (b) The trapped atoms are then transferred into a deep, large volume optical dipole trap that is created using an optical resonator. In the next step, the atoms are transferred into a tightly focused optical tweezer. (c) By moving a lens, the atoms in the optical tweezer are transported into the octagonal glass cell which offers exceptional optical access. (d) Here, optical evaporation is performed by decreasing the power in the optical tweezer, resulting in the formation of an ultracold Fermi gas.

curvature: 15 cm) in hemi-spherical configuration, and has a finesse of 10200, a resonator length of 14.975 cm, a free spectral range of 1 GHz and a power enhancement factor of 1580. The resonator trap is driven by far off-resonant laser light at a wavelength of 1064 nm and reaches a maximum trap depth of about  $500 \mu\text{K}$  for a waist of  $500 \mu\text{m}$  ( $1/e^2$ -radius) at the MOT position. Here, the atomic sample, which equally populates the two lowest hyperfine sub-states of  ${}^6\text{Li}$ , is evaporatively pre-cooled. During the evaporation, we apply a magnetic field of 300 G to set the s-wave scattering length for the interstate collisions of the two hyperfine sub-states to  $-300 a_0$ , where  $a_0$  is the Bohr radius. The resonator trap serves as intermediate trapping potential [24], which maximizes the particle transfer from the MOT into the final trapping configuration, a tightly focused optical tweezer (waist  $w = 21 \mu\text{m}$ ), also at a wavelength of 1064 nm. Typically, about  $1.5 \times 10^6$  atoms in each sub-state are transferred from the resonator trap into the running wave optical dipole trap, which has a maximum initial trap depth

of  $\sim 150 \mu\text{K}$ . By moving a lens over a distance of 26.88 cm [25], the atoms in the optical tweezer are then transported into the octagonal UHV glass cell (see figure 1(c)). Here, forced evaporation is performed by decreasing the power in the optical tweezer from 2 W down to a few mW, also at a magnetic field of 300 G (see figure 1(d)). This results in the formation of a quantum degenerate Fermi gas of  $3 \times 10^5$  atoms in each of the two lowest hyperfine sub-states at a relative temperature of  $\sim 0.3 T_F$ , where  $T_F$  is the Fermi temperature. For the experiments shown in this paper, we typically prepare the sample at this temperature.

### 3. Optical system

The main feature of the experimental setup is the high-resolution optical system as illustrated in figure 2, with two identical microscope objectives centered along a common optical axis: one above the glass cell, allowing for shaping optical dipole potentials down to length scales below one micrometer; the other below the glass cell, used for high-resolution imaging of the trapped quantum gas. We first describe the technical details of the microscope objectives, before discussing their applications for the microscopic imaging and manipulation of ultracold fermions.

#### 3.1. High-resolution microscope objectives

Each of the two identical, long-working-distance microscope objectives (SPECIAL OPTICS, Inc.) is based on a system of 7 lenses as depicted in figure 2. The infinite-conjugate configuration is designed for three operating wavelengths at 532 nm, 671 nm and 770 nm, correcting aberrations of all three wavelengths. Furthermore, the objectives are corrected for a view through the 4 mm thick quartz window of the glass cell. Each objective has an effective focal length of  $f_{\text{eff}} = 18 \text{ mm}$ , and covers a numerical aperture of  $\text{N.A.} = 0.53$ . This yields a theoretical diffraction limit of 650 nm (full-width at half-maximum, FWHM) for an imaging wavelength of 671 nm. All optical surfaces are anti-reflection coated for the above wavelengths (reflectivity  $R < 0.75\%$ ) and additionally for 1064 nm ( $R < 2.0\%$ ). The lenses are mounted in a non-magnetic and non-conducting housing made of Ultem 3000 allowing for an undisturbed operation in the vicinity of the magnetic coils around the glass cell.

We achieve the specified maximum optical performance at the diffraction limit (RMS wavefront error  $< 7\%$  of the wavelength) by an accurate alignment of each microscope objective. The required constraints for the absolute position accuracy only allow a displacement from the optical axis by less than 1 mm, a de-focussing smaller than  $3 \mu\text{m}$ , and a tilt of the microscope axis with respect to the normal of the glass cell below  $0.1^\circ$ . To meet these conditions the mounting of the microscope objective includes a coarse and fine adjustment along five axes. The tilting along two perpendicular axes can be adjusted with a goniometer (NEWPORT, M-TTN80) without altering the height of the mount along the central axis. This tilt platform has a central aperture with an

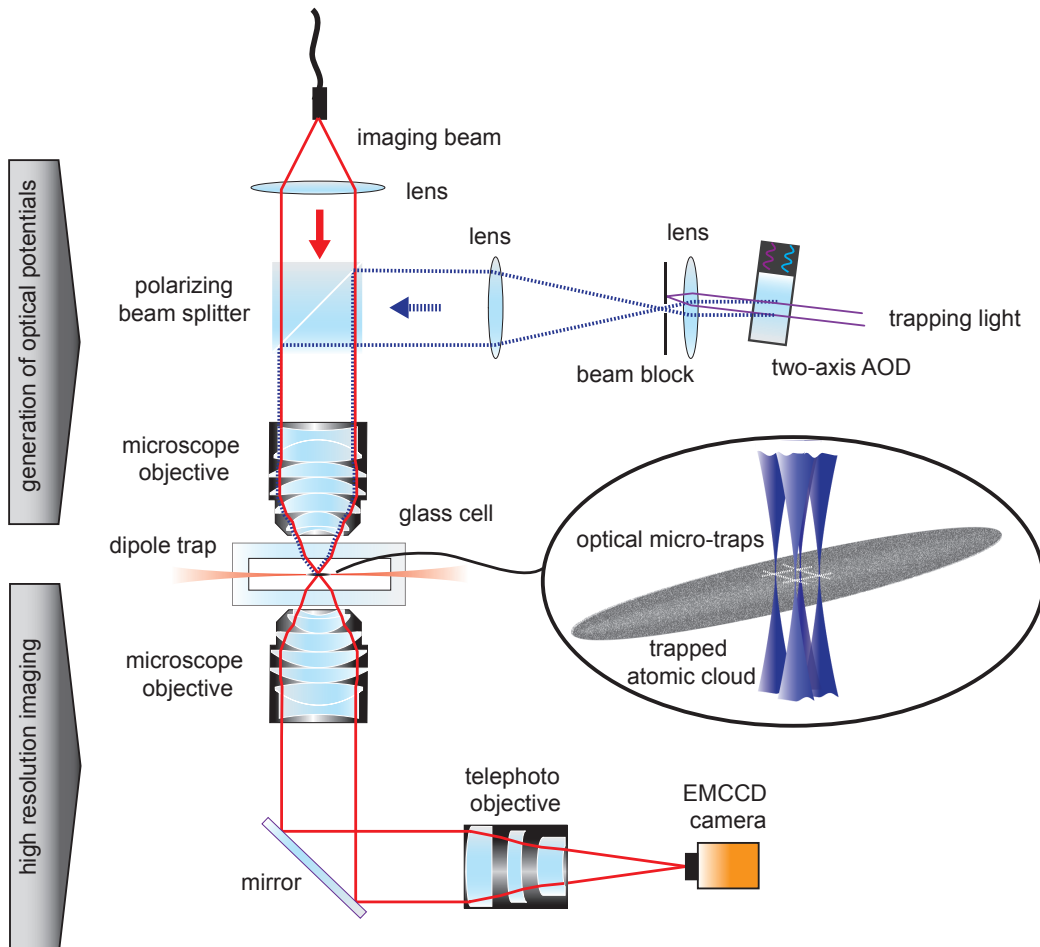


**Figure 2.** Two identical microscope objectives with high numerical aperture constitute the heart of the high-resolution optical system: The microscope objective below the glass cell and the telephoto objective belong to the high-resolution imaging setup. Probe light, resonant to the  $|2S_{1/2}\rangle$  to  $|2P_{3/2}\rangle$  transition along the D2-line of  ${}^6\text{Li}$ , is collected by the microscope objective and imaged on an electron-multiplying CCD camera (EMCCD). The second microscope objective is part of the optical system for generating arbitrary optical micro-potentials. A two-axis acousto-optical deflector generates several, far off-resonant laser beams in a programmable way. Each of those beams is focussed by the microscope objective, resulting in a controllable pattern of multiple optical tweezers in the focal plane (see inset). The setup allows for static as well as for time-averaged or dynamical optical potentials.

inside thread holding the microscope tube, which is made of machinable glass-ceramic (MACOR). This permits a coarse focussing of the microscope objective in axial direction ( $750\ \mu\text{m}$  per revolution). The transversal coarse adjustment is performed by a two-axis translation stage (OWIS, KT90), also with a central aperture. For the fine adjustment in transversal and axial direction we use a compact, piezo-driven three-dimensional translation stage (Piezo Jena, Tritor 102 SG EXT) with a maximum translation distance of  $100\ \mu\text{m}$  and a resolution of  $3\ \text{nm}$ . This device includes a strain gauge to measure the

absolute position along each axis. Via a digital proportional-integral controller based on a field programmable gate array (National Instruments, NI 9264/9205/9401) the error in position can be fed back to the piezo stage to actively stabilize the transversal and axial position of the setup. The passive stability of the goniometer is sufficient to keep the tilt angles within the constraints.

### 3.2. Imaging setup

The high-resolution imaging system is sketched in the lower part of figure 2, underneath the glass cell. It consists of three components along the optical axis: The lower microscope objective, a telephoto objective and an electron-multiplying CCD camera (EMCCD). The custom-made telephoto objective (SPECIAL OPTICS, Inc.) is an infinite-conjugate design with a focal length of approximately 1 m. The 3-lens system is modeled for a joint operation with the microscope objective at the diffraction limit and also corrects aberrations at 532 nm, 671 nm and 770 nm. The lens surfaces of the telephoto objective are AR-coated for the same wavelengths as the microscope objective. The microscope objective is mounted 1.2 mm below the glass cell, followed by the telephoto objective at a distance of about 430 mm. The EMCCD camera is placed in the focal plane of the telephoto objective, about 450 mm behind its last lens. In total, the imaging system yields a magnification factor of 54 and a field of view of  $100 \mu\text{m} \times 100 \mu\text{m}$ . In a calibration measurement [26], the optical resolution was determined to be about 660 nm (FWHM) for a wavelength of 671 nm. The depth of field at full resolution is limited to  $3.5 \mu\text{m}$ , while the measured chromatic axial focal shift was found to be well below 500 nm for the above wavelengths. For the detection of the imaging light we use a back-illuminated EMCCD camera (ANDOR, iXon 897). Due to the magnification factor of 54, each pixel ( $16 \mu\text{m} \times 16 \mu\text{m}$ ) thus corresponds to  $\sim 300 \text{ nm} \times 300 \text{ nm}$  in the object plane. Using the electron multiplier detected signals on the level of a few incoming photons are amplified well above the read-out noise of the CCD camera.

### 3.3. Generation of optical micro-potentials

We now describe the concept and setup for the creation of static and time-averaged optical dipole potentials used to trap small samples of a cold atomic gas. Similar to other work [19, 18, 27, 28], we employ a two-axis acousto-optical deflector (AOD) for the generation of structured optical trap configurations. The AOD deflects and frequency shifts a red-detuned laser beam proportionally to the frequency of the RF (radio-frequency) field fed into the AOD, while its intensity can be controlled by the amount of RF power. The deflected beam - enlarged by telescope optics - is then focussed by the upper microscope objective onto the atomic cloud trapped in the large transport dipole trap. Different deflection angles result in different positions of the tweezer in the focal plane of the microscope objective as the latter works as a Fourier transformer. The two-dimensional AOD is able to deflect along two orthogonal axes and can be driven by multiple RF frequencies along each axis at the same time. By this, versatile two-

dimensional multiple beam patterns can be created resulting from the convolution of the beams deflected along the two perpendicular directions (see inset of figure 2).

Our setup for generating multiple optical micro-potentials is sketched in the upper part of figure 2, above the glass cell. As AOD we use a two-axis deflector (IntraAction Corp., Model A2D-603AHF3A, center frequency 60 MHz, 3 mm aperture) which incorporates a special acoustic phased-array beam-steering design in order to maintain a uniform diffraction efficiency (80%) across the deflection bandwidth of 30 MHz (values for operation on only one axis). Additionally, a short access time ( $\sim 276$  ns/mm beam diameter) of the AOD allows for the creation of time-averaged potentials (see section 4). A collimated laser beam (waist 1.2 mm) at a wavelength of 767 nm enters the AOD and is subsequently deflected into the (-1<sup>st</sup>/-1<sup>st</sup>)-order for each applied RF frequency. The deflected beams are then expanded by a two-lens telescope to a maximum waist of 12.5 mm. The microscope objective finally focusses these collimated beams down to a diffraction limited spot size of about 730 nm. With the opto-mechanical mounting for the microscope objective described above, the resulting micro-trap pattern can be precisely aligned and position-stabilized onto the atomic sample in the transport dipole trap (see inset of figure 2). As RF-source we employ a Universal-Software-Radio-Peripheral-2, which is controlled via the gnuradio-software [29, 30]. It is capable of generating arbitrary wave forms with a bandwidth of 25 MHz around a central frequency (60 MHz).

#### 4. Optical micro-potentials

The configuration of our optical system with the two identical microscopes allows us to directly monitor the optical potential landscape: the high-resolution imaging setup below the glass cell accurately maps the position, dimensions and intensity distribution of the trapping light pattern shaped by the optical setup above the glass cell. Using this information, we are able to characterize the trap geometry in terms of waists, spacings, trap depths and trap frequencies. Moving the imaging setup out of the focus of the upper microscope also provides insight into trap parameters along the beam propagation direction.

##### 4.1. Single spot micro-trap

Figure 3(a) shows the focal, two-dimensional intensity distribution of a single spot created by the upper microscope as it is imaged with high resolution by the lower microscope onto the EMCCD camera. Fitting a Gaussian function to the measured intensity profiles along the x- and y-axis yields a spot size with a waist ( $1/e^2$ -radius) of  $w_x = 734$  nm, and  $w_y = 726$  nm respectively (see figure 3(b)). By moving the imaging system along the beam propagation direction we measure the longitudinal intensity profile which allows us to extract the Rayleigh length of the micro-trap. For the given example in figure 3(a) the Rayleigh length is measured to be  $\sim 2.1$   $\mu$ m. With

these parameters and a light power of 0.1 mW, an optical dipole trap with a calculated depth of  $18.6 \mu\text{K}$  for  ${}^6\text{Li}$  atoms is created. The corresponding trapping frequencies in radial direction are  $\omega_x = 2\pi \cdot 69.5 \text{ kHz}$  and  $\omega_y = 2\pi \cdot 70.2 \text{ kHz}$ , and  $\omega_z = 2\pi \cdot 16.5 \text{ kHz}$  along the axial confinement. A Gaussian trap is well approximated by a harmonic potential up to 20% of the trap depth, whereas the total number of states in a harmonic trapping potential at zero temperature with energy less than  $\varepsilon$  is given by  $G(\varepsilon) = \frac{1}{6} \frac{\varepsilon^3}{\hbar^3 \omega_x \omega_y \omega_z}$ . According to this, for 0.1 mW light power the single-spot dipole trap only offers approximately one available state up to an energy level of 20% of its trap depth. However, when we load atoms into the micro-potential (see section 5), nearly all energy levels up to the edge of the trap depth are populated. For the given parameters, an interpolating expression [31] for the number of single particle eigenstates of a Gaussian trap yields about 700 available states up to 99% of the trap depth.

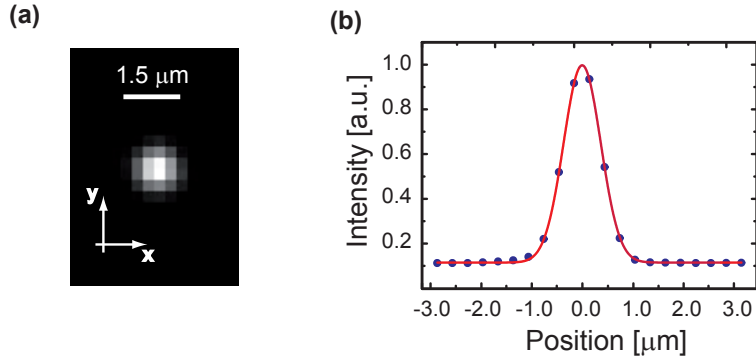


**Figure 3.** (a) High-resolution image of a single-spot dipole trap in its focal plane (wavelength 767 nm), illustrating the capability of the optical system to map and characterize the optical potential landscape. For the imaging, a bandpass filter for 671 nm light in front of the CCD camera is removed which normally blocks the trapping light in the infra-red (767 nm) when only the atoms trapped in the optical potential are to be imaged. (b) Intensity profile of the single spot along the  $x$ -axis. A Gaussian fit to the two-dimensional intensity distribution yields the corresponding waists of the micro-trap.

#### 4.2. Multiple spot micro-traps

Figure 4 and figure 5 illustrate a selection of possible multiple-spot potential patterns realized with our setup. The images are again direct maps of the potentials in their focal plane, imaged onto the EMCCD camera.

*Two-dimensional finite optical lattice* Applying four RF frequencies to each axis of the 2D AOD at the same time results in a static 4x4 beam diffraction pattern in the -1<sup>st</sup>/-1<sup>st</sup>-diffraction order. In the focal plane of the upper microscope, this pattern yields a square array of 4x4 dipole traps which forms a finite-size, homogenous 2D optical lattice system. Figure 4(a) shows such a lattice configuration. Here, the four applied RF frequencies are

symmetrically arranged around the center frequency of 58 MHz, separated by 7 MHz. In real space, this corresponds to a lattice site separation of approximately  $3 \mu\text{m}$  in the focal plane. Smaller lattice spacings can be achieved with smaller RF frequency separations (figure 4(b-e)). The spatial resolution of the imaging systems allows us to resolve lattice spacings down to one micrometer as can be seen in figure 4(e). The spacing can be changed dynamically even during one experimental cycle, thus enabling e.g. the tuning of tunneling dynamics within one experiment. Increasing the number of applied RF frequencies easily enlarges this two-dimensional lattice pattern to a maximum of  $8 \times 8$  sites, limited by the finite RF deflection bandwidth of the 2D AOD. For the given configuration in figure 4(e), with a lattice spacing of  $1.2 \mu\text{m}$  and  $10 \mu\text{W}$  light power per lattice site, we estimate a tunneling rate of about 800 Hz for  ${}^6\text{Li}$  atoms populating the lowest Bloch band. These substantial tunneling rates in combination with the possibility to tune the interparticle interactions via Feshbach resonances thus provide a prospect for the realization of Hubbard-model like physics in a finite-size, homogenous lattice system.

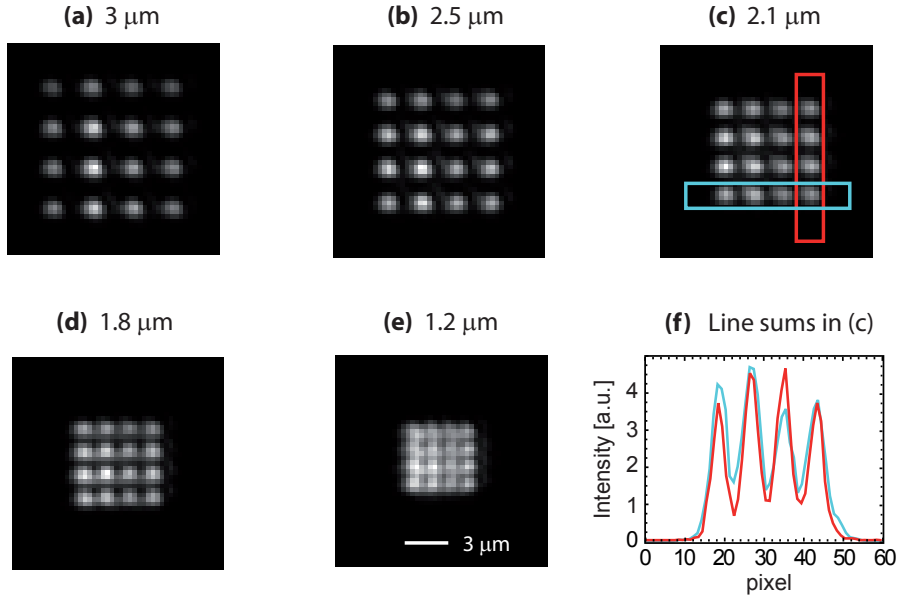


**Figure 4.** High-resolution images of a  $4 \times 4$  site 2D lattice configuration with different lattice spacings: (a)  $3 \mu\text{m}$ , (b)  $2.5 \mu\text{m}$ , (c)  $2.1 \mu\text{m}$ , (d)  $1.8 \mu\text{m}$ , and (e)  $1.2 \mu\text{m}$ . Each lattice site has a Gaussian spot size of approximately  $800 \text{ nm}$  ( $1/e^2$ -radius). This spot size is slightly larger than for the single spot shown in figure 3 since here, as well as for the ring lattice shown in figure 5, the numerical aperture of the upper microscope was reduced facilitating the alignment for this first demonstration. (f) Vertical and horizontal line sum profiles of the selected region in (c), marked in blue and red, respectively. The partial inhomogeneity in the intensity of different lattice sites results from an inhomogeneous diffraction efficiency within the RF bandwidth of the two-axis AOD. This inhomogeneity can be minimized, since the RF power for each RF frequency can be individually controlled, independently for both axes.

*Ring lattice* Apart from static potentials, our setup also allows us to generate time-averaged optical potentials by alternately projecting different trapping geometries onto the atoms. For this, the switching rate between the different trap configurations has to exceed the corresponding trapping frequency significantly in order to display a static trapping potential for the atoms. In figure 5 we give an example of such a time-averaged optical potential. Here, we switch periodically with a frequency of 500 kHz between two different rectangular 2x2 lattice configurations. This results in a 8-site ring lattice structure as schematically sketched in figure 5(a). Figure 5(b) presents the realization of this ring lattice with our setup, showing the corresponding light intensity distribution in the focal plane. In the given case, the ring diameter measures  $\sim 6.9 \mu\text{m}$  with a Gaussian spot size of approximately 800 nm ( $1/e^2$ -radius) for each lattice site. For the ring lattice the site separation can also be controlled arbitrarily down to about one micrometer as demonstrated for the square lattice configuration in the previous section.

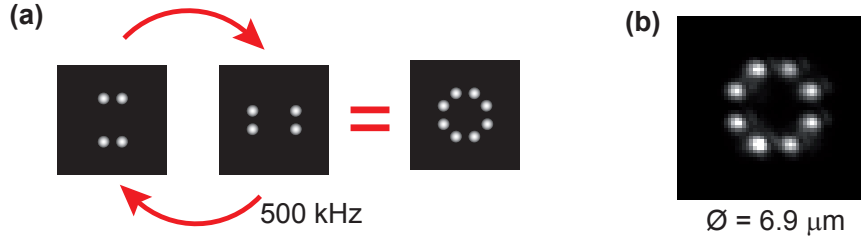


**Figure 5.** (a) Simulation data illustrating the generation of a time-averaged ring lattice: two 2x2 rectangular square lattices - arranged perpendicular to each other around a common symmetry axis - are alternately projected onto the atoms. The switching frequency between the two configurations is 500 kHz, well above the trapping frequency of each individual lattice site. (b) Real data image showing the light intensity distribution of the resulting 8-site ring lattice with a diameter of  $6.9 \mu\text{m}$ .

## 5. Atoms in micro-potentials

The micro-trap patterns are filled from the reservoir of cold atoms captured in the optical dipole trap which is used for the transport and the final evaporative cooling in the glass cell. For this, the transport and the micro-traps are spatially superimposed as sketched in the inset of figure 2. Illustrating this situation, figure 6(a) shows an in-situ absorption image of the center part of an atomic sample held in the transport dipole trap (black region). On top, a 4x4 lattice is imprinted whose intensity distribution is simultaneously imaged, here appearing as white dots. For the transfer of atoms, we smoothly ramp up the power of the micro-trap potential to its final value (about  $100 \mu\text{W}$  per site) in 200 ms and then switch off the transport trap rapidly.

Imaging atoms in the micro-traps is challenging as the individual tightly focussed laser beams spatially overlap at a certain distance along the axial direction, depending on their separation. Moreover, the atoms typically populate energy levels up the edge

of the trap right after the transfer. Therefore, by resonant absorption imaging along the microscope axis the individual atomic samples in different trapping potentials appear as a continuous shadow cast on the CCD camera. However, the filling of the micro-traps can be reduced by sending resonant light onto the atoms prior to the imaging. For this purpose, we apply a resonant light pulse of  $4\ \mu\text{s}$  at one tenth of the  ${}^6\text{Li}$  saturation intensity ( $2.54\ \text{mW}/\text{cm}^2$ ) onto the sample. This removes the atoms in trap regions of shallow potential depth and only leaves atoms in the tightly confining center. By a second resonant light pulse ( $24\ \mu\text{s}$ ) at twice the saturation intensity, the remaining atoms are then imaged through the microscope setup onto the CCD camera. Figure 6(b) shows the in-situ absorption image of the remaining atoms trapped in a  $4\times 4$  two-dimensional square lattice with a site separation of  $2.5\ \mu\text{m}$ .

Alternatively, due to the high optical density, the atoms can be imaged dispersively with off-resonant laser light, which reveals the atoms captured in the center of each micro-trap. For this, we red-detune the imaging light along the  $|2S_{1/2}\rangle$  to  $|2P_{3/2}\rangle$  transition by about  $10\Gamma$  with respect to the second lowest hyperfine sub-state of  ${}^6\text{Li}$ . Here,  $\Gamma = 5.9\ \text{MHz}$  is the natural line width of the D2 transition of  ${}^6\text{Li}$ . The resulting off-resonant dispersive image can be seen in figure 6(c) where the atoms in the different trap centers of the  $4\times 4$  lattice appear as well separated dark spots. In this case, a preparatory resonant light pulse in advance is not required. We applied the same off-resonant imaging technique to atoms trapped in the 8-site ring lattice structure (figure 5(b)), see figure 6(d).

The number of trapped atoms can be estimated in a time of flight (TOF) measurement: Releasing the sample from the confining optical potential the expanding cloud is imaged after a certain TOF by means of resonant absorption imaging through the microscope. From a fit to the detected density profile we determine the total atom number. For the situation in figure 6(c), the fit yields an upper limit of 300 atoms per lattice site. We also measured the lifetime of the trapped sample in a separate experiment. For the static potential we observe a two-stage loss process of the trapped atoms. In an initial fast decay on a short timescale ( $\sim 100\ \text{ms}$ ), the atom number is approximately reduced by a factor of 2. Subsequently, the population decays exponentially on a longer timescale, yielding a lifetime of 800 ms. For the time-averaged ring lattice, we find shorter lifetimes of about 100 ms. A recent measurement of inelastic collisions in a two-component Fermi gas prepared in the strongly interacting BEC-BCS crossover [32] showed that two- and three-body collisions give rise to particle losses on a time scale well above one second. Our samples have a comparable density, yet are weakly interacting ( $a = -300\ a_0$ ) and hence the effect of three-body collisions on the observed lifetime are expected to be negligible. In addition, we can exclude light scattering to affect the lifetime of the trapped sample. For the given trap parameters, the photon scattering rate is 0.25 Hz per atom. Most likely, the particle loss is caused by free evaporation from the initially completely filled micro-traps. Moreover, the intensity of the micro-trap was not actively stabilized for the presented measurement, possibly causing spilling of particles from the trap due to fluctuations in the trap depth. The even

faster loss rates observed for the ring lattice potential are probably induced by heating of the sample due to the fact that this particular trapping configuration results from a time averaged projection of two rectangular lattice patterns. Further investigation is needed to fully understand the observed lifetimes.

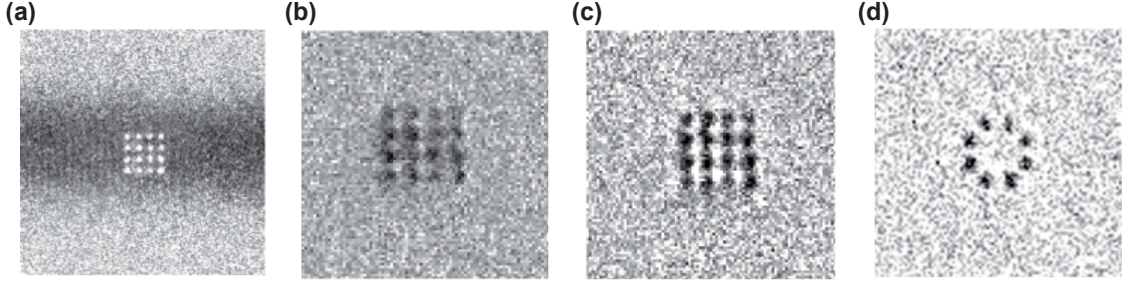


**Figure 6.** (a) 4x4-site 2D optical lattice superimposed to a fermionic atom cloud trapped in the transport dipole trap. For this image, the bandpass filter for 671 nm in front of the CCD camera was removed, allowing to image both, the trapped atom cloud with resonant absorption imaging at 671 nm and the focal light intensity distribution of the 4x4 lattice at 767 nm. (b) Resonant absorption image of atoms trapped in the lattice structure after a preparatory resonant light pulse was applied which removed atoms in the shallow trapping regions. (c) Off-resonant imaging of the same system, red-detuned by  $\sim 10\Gamma$  with respect to the upper hyperfine ground state of  ${}^6\text{Li}$  (illumination time:  $12\ \mu\text{s}$ ). (d) Equivalent red-detuned imaging of atoms trapped in the 8-site ring lattice pattern given in figure 5. All images are divided by a reference image taken without atoms being present.

## 6. Conclusion and outlook

We have presented an experimental setup with two high-resolution microscope objectives that allows us to optically probe and prepare an ultracold Fermi gas on the microscopic length scale of the Fermi wavelength. Employing a 2D acousto-optical deflector, we have demonstrated the site-by-site generation of a finite two-dimensional square lattice and a 8-site ring lattice configuration. Moreover, we have shown the capability to load small numbers of atoms into these optical micro-potentials and to detect them with single-site resolution.

An immediate, although non-trivial extension of this work would be the measurement of the temperature in the micro-traps. Currently, the measured particle numbers and the known trap geometry should lead to a Fermi temperature close to the trap depth which gives us confidence in the assumption that the trapped sample might be quantum degenerate.

The expected substantial tunneling amplitudes for  ${}^6\text{Li}$  atoms in combination with the possibility to tune the inter-particle interactions via Feshbach resonances promises a possible realization of Hubbard-model like physics beyond the standard optical lattice approach with interfering laser beams. While the site-by-site creation of lattice sites has

the advantage of the intrinsic absence of additional external confinement, it also offers the ability to generate lattice systems of low symmetry or systems with inherent defects. In addition, our setup holds the potential for a single-site addressability allowing the individual manipulation of atoms in different trap spots [12, 21, 33, 34].

## Acknowledgments

We acknowledge J.-P. Brantut and D. Stadler for experimental assistance and valuable discussions. We also thank the group of M. Oberthaler (Heidelberg) for the loan of a test target. This work was supported by the ERC advanced grant SQMS, the FP7 FET-open grant NameQuam and the NCCR MaNEP. Mention of industrial brand names is for technical communication only and does not constitute an endorsement of such products.

## References

- [1] Inguscio M, Ketterle W and Salomon C (eds) 2008 *Ultra-cold Fermi Gases: Proceedings of the International School of Physics "Enrico Fermi", Course CLXIV 2006* (Societa italiana di fisica)
- [2] Nelson K, Li X and Weiss D 2007 *Nature Phys.* **3** 556–560
- [3] Gericke T, Würtz P, Reitz D, Langen T and Ott H 2008 *Nature Phys.* **4** 949–953
- [4] Bakr W S, Gillen J I, Peng A, Fölling S and Greiner M 2009 *Nature* **462** 74–77
- [5] Müller T, Zimmermann B, Meineke J, Brantut J P, Esslinger T and Moritz H 2010 *Phys. Rev. Lett.* **105** 040401
- [6] Recati A and Stringari S 2010 *arXiv* **1007.4504**
- [7] Sanner C, Su E J, Keshet A, Huang W, Gillen J, Gommers R and Ketterle W 2011 *Phys. Rev. Lett.* **106** 010402
- [8] Yang C N 1962 *Rev. Mod. Phys.* **34** 694–704
- [9] Bloch I 2005 *Nat Phys* **1** 23–30
- [10] Jaksch D and Zoller P 2005 *Ann. Phys.* **315** 52–79
- [11] Esslinger T 2010 *Annual Review of Condensed Matter Physics* **1** 129–152
- [12] Würtz P, Langen T, Gericke T, Koglbauer A and Ott H 2009 *Phys. Rev. Lett.* **103** 080404
- [13] Bakr W S, Peng A, Tai M E, Ma R, Simon J, Gillen J I, Fölling S, Pollet L and Greiner M 2010 *Science* **329** 547–550
- [14] Sherson J F, Weitenberg C, Endres M, Cheneau M, Bloch I and Kuhr S 2010 *Nature* **467** 68–72
- [15] Albiez M, Gati R, Fölling J, Hunsmann S, Cristiani M and Oberthaler M K 2005 *Phys. Rev. Lett.* **95** 010402
- [16] Boyer V, Godun R M, Smirne G, Cassettari D, Chandrashekar C M, Deb A B, Laczik Z J and Foot C J 2006 *Phys. Rev. A* **73** 031402
- [17] Heathcote W H, Nugent E, Sheard B T and Foot C J 2008 *New Journal of Physics* **10** 043012
- [18] Henderson K, Ryu C, MacCormick C and Boshier M G 2009 *New Journal of Physics* **11** 043030
- [19] Schnelle S K, van Ooijen E D, Davis M J, Heckenberg N R and Rubinsztein-Dunlop H 2008 *Optics Express* **16** 1405–1412
- [20] Meyrath T P, Schreck F, Hanssen J L, Chuu C S and Raizen M G 2005 *Phys. Rev. A* **71** 041604
- [21] Dumke R, Volk M, Müther T, Buchkremer F B J, Birkl G and Ertmer W 2002 *Phys. Rev. Lett.* **89** 097903
- [22] Zimmermann B 2010 *Microscopy of ultracold fermionic lithium* Ph.D. thesis ETH Zurich, Diss. ETH No. 19085

- [23] Jochim S, Bartenstein M, Altmeyer A, Hendl G, Riedl S, Chin C, Denschlag J H and Grimm R 2003 *Science* **302** 2101–2103
- [24] Mosk A, Jochim S, Moritz H, Elsässer T, Weidemüller M and Grimm R 2001 *Optics Letters* **26** 1837–1839
- [25] Gustavson T L, Chikkatur A P, Leanhardt A E, Görlitz A, Gupta S, Pritchard D E and Ketterle W 2001 *Phys. Rev. Lett.* **88** 020401
- [26] Ottenstein T 2006 *A new objective for high resolution imaging of Bose-Einstein condensates* Master's thesis Kirchhoff Institute of Physics, Heidelberg
- [27] Friedman N, Khaykovich L, Ozeri R and Davidson N 2000 *Phys. Rev. A* **61** 031403
- [28] Onofrio R, Durfee D S, Raman C, Köhl M, Kuklewicz C E and Ketterle W 2000 *Phys. Rev. Lett.* **84** 810–813
- [29] GNU radio project, USRP documents URL <http://gnuradio.org/trac/wiki/USRP>
- [30] GNU radio project, software and instructions URL <http://gnuradio.org/trac>
- [31] Simon L and Strunz W T 2010 *Phys. Rev. A* **81** 063620
- [32] Du X, Zhang Y and Thomas J E 2009 *Phys. Rev. Lett.* **102** 250402
- [33] Scheunemann R, Cataliotti F S, Hänsch T W and Weitz M 2000 *Phys. Rev. A* **62** 051801
- [34] Karski M, Frster L, Choi J M, Steffen A, Belmechri N, Alt W, Meschede D and Widera A 2010 *New Journal of Physics* **12** 065027